Nano Research

Open Access

Research Article

Polysaccharide-engineered selenium nanoparticles regulate the Trx1/TrxR1 antioxidant axis to scavenge ROS and drive osteogenesis of midpalatal sutures in rapid maxillary expansion

Ying Liang[§], Ting Liu[§], UnMan Chan, Yuzheng Xie, Rong Deng, Xun Wang, Qi Feng, Tianfeng Chen ✉, and Yue Huang ✉

School of Stomatology, Department of Chemistry, Jinan University, Guangzhou 510632, China
[§] Ying Liang and Ting Liu contributed equally to this work.

Cite this article: *Nano Research*, **2026**, *19*, 94908704. https://doi.org/10.26599/NR.2026.94908704

ABSTRACT: Rapid maxillary expansion (RME) is an effective approach for addressing maxillary transverse deficiency; however, it is prone to recurrence owing to insufficient bone remodeling within the maxilla midpalatal suture (MPS). Clinically established drug therapies or auxiliary interventions capable of reliably promoting osteogenesis in RME remain absent. As a potent antioxidant, selenium can decrease reactive oxygen species (ROS) production to influence bone metabolism and formation to promote remodeling. In this study, we propose the application of lentinan-engineered selenium nanoparticles (LET-SeNPs) in RME to accelerate bone formation in MPS. The results demonstrate that LET-SeNPs are capable of enhancing the proliferative capacity of rat bone marrow mesenchymal stem cells (rBMSCs) and facilitating their osteogenic differentiation. Furthermore, LET-SeNPs eliminate ROS via the thioredoxin/thioredoxin reductase 1 (Trx1/TrxR1) system and suppress oxidative stress, thereby augmenting the antioxidant capacity of rBMSCs. In a rat RME model, local injection of LET-SeNPs can accelerate bone formation in MPS by enhancing osteoblast activity and inhibiting osteoclast expression while simultaneously accelerating new bone maturation in MPS. In conclusion, the results of this study suggest that local injection of LET-SeNPs is a promising therapeutic intervention for improving the therapeutic efficacy of RME.

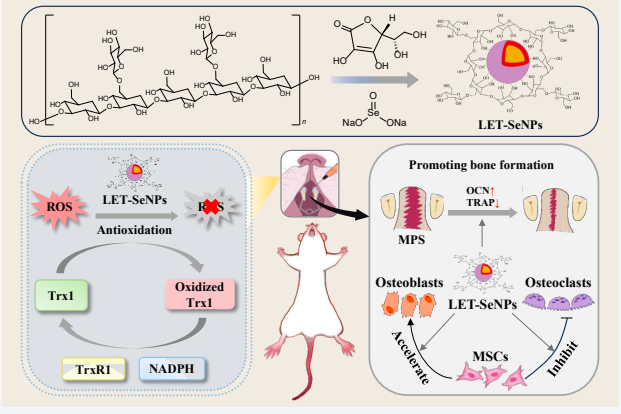

KEYWORDS: selenium nanoparticles, thioredoxin (TrxR1), oxidative stress, osteogenesis, rapid maxillary expansion

1 Introduction

In recent years, maxillary transverse deficiency (MTD), also known as insufficient maxillary transverse development caused by congenital malformations or postnatal factors, has become a common clinical malocclusion, with an incidence rate of up to 9.4% in adults and 23.3% in deciduous and mixed dentition periods [1]. Its clinical manifestations include crowded teeth, a narrow dental arch, a highly vaulted palate, labial inclination of incisors, and reverse bite of the posterior teeth [2]. MTD causes different degrees of harm to oral function, facial beauty, and physical and mental health. Rapid maxillary expansion (RME) is one of the most important approaches for MTD treatment [3, 4]. RME involves swift exertion of force on the midpalatal suture (MPS) using an expansion apparatus to expand MPS, widen the basal bone and dental arch, and facilitate new bone formation [5, 6]. Despite the favorable osteogenic induction effect of RME, it requires a relatively long stabilization period, which discomforts patients and is accompanied by tooth tilting and root resorption [7] and other complications [8]. Furthermore, owing to failure to establish a new equilibrium in the surrounding oral muscle groups after expansion and insufficient bone remodeling in MPS, RME has a relatively high recurrence rate [9]. Accelerating bone formation in MPS shortens the retention period, thereby enabling bones to effectively resist recurrence [10, 11]. Consequently, investigating how to

Received: January 26, 2026; **Revised:** March 31, 2026
Accepted: April 2, 2026

✉Address correspondence to Tianfeng Chen, tchentf@jnu.edu.cn; Yue Huang, yue-huang@hotmail.com

accelerate bone tissue remodeling during expansion and shorten the treatment cycle is crucial for preventing and reducing recurrence [12].

Bone remodeling is an intricate process characterized by the breakdown of damaged bone tissue via osteoclast-mediated resorption, which is followed by new bone generation via the activity of osteoblasts [13]; it is influenced by reactive oxygen species (ROS). MPS expansion results in increased metabolism, which augments ROS production and triggers oxidative stress (OS), thereby enhancing osteoclast function and inhibiting osteoblast differentiation [14, 15]. Selenium, an important trace element with a 16% content in human bones [16], influences bone metabolism and formation [17]. As a potent antioxidant, Se can decrease ROS production [18]; it has a substantial impact on bone remodeling [19]. Selenium nanoparticles (SeNPs) exist in elemental form and possess lower toxicity than inorganic and organic Se. They also exhibit numerous advantages, such as high bioavailability, high reaction yield, and surface modification feasibility [20, 21]. In previous studies, SeNPs demonstrated outstanding osteogenic capacity. SeNPs stimulate cells to differentiate into osteoblast lineages, facilitate bone formation [22, 23], and even inhibit osteoclast formation and activity [24–26]. SeNPs are gradually being used in clinical treatments, including routine trace-element supplementation and management of diseases such as cancer, diabetes, hypertension, and osteoporosis [27–29].

However, existing SeNPs are prone to aggregation in biological environments. Once nanoparticles aggregate, the biological activity of SeNPs is significantly reduced. Lentinan (LET) was selected over other polysaccharides for three key reasons. First, it possesses an exceptionally hydroxyl-rich β-glucan structure that forms strong intermolecular interactions with Se atoms, enabling precise control over the nucleation and growth of SeNPs and effectively preventing aggregation in biological environments [30]. Second, LET possesses well-documented biocompatibility, biodegradability, and immunomodulatory properties, rendering it a safe surface modifier for *in vivo* applications. Third, LET exhibits intrinsic osteogenic-supportive and anti-inflammatory activities, which may act synergistically with Se to promote bone remodeling [31, 32]. These combined advantages make LET a more suitable choice than other polysaccharides such as chitosan or polyethylene glycol, which lack this specific combination of structural Se compatibility and osteogenic relevance. Consequently, in this study, we employed stable and well-dispersed LET-SeNPs that could be mass-produced to explore whether they facilitated bone formation in RME. H_2O_2 was used to induce OS. The protective effect of LET-SeNPs against oxidative damage in rat bone marrow mesenchymal stem cells (rBMSCs) and their effect on the *in vitro* osteogenesis of rBMSCs were investigated. Moreover, using *in vivo* animal experiments, the influence of local application of LET-SeNPs on new bone formation in MPS of a rat RME model was observed and analyzed, providing a theoretical basis for enhancing the effect of RME using LET-SeNPs (Scheme 1).

2 Results and discussion

2.1 Synthesis and characterization of LET-SeNPs

LET-SeNPs are SeNPs synthesized with LET as a modifier; they form a spherical structure owing to intermolecular interaction between the closed-ring structure of LET and Se atoms (Fig. 1(a)). Dynamic light scattering (DLS) characterization showed that the potential and hydrodynamic size of LET-SeNPs were approximately −20 mV and 110.2 nm (PDI = 0.199), respectively (Fig. 1(b)). Simultaneously, transmission electron microscopy

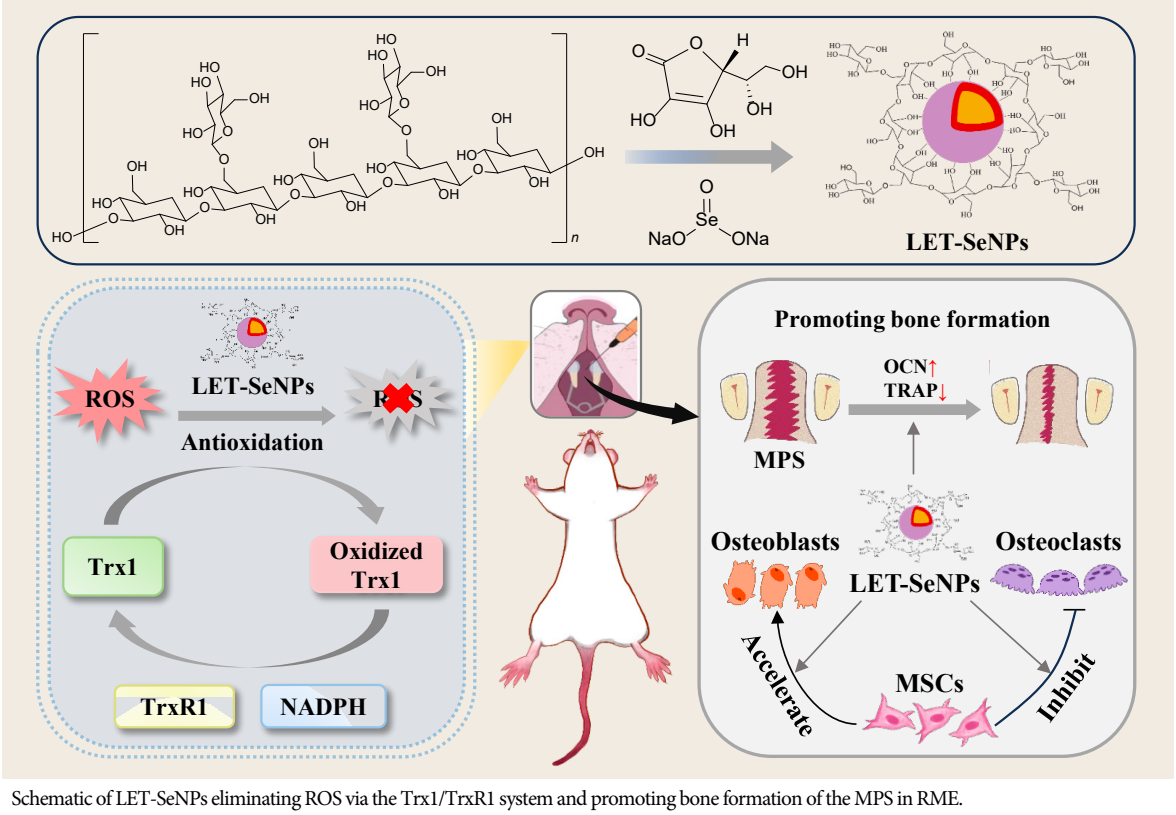

Scheme 1 Schematic of LET-SeNPs eliminating ROS via the Trx1/TrxR1 system and promoting bone formation of the MPS in RME.

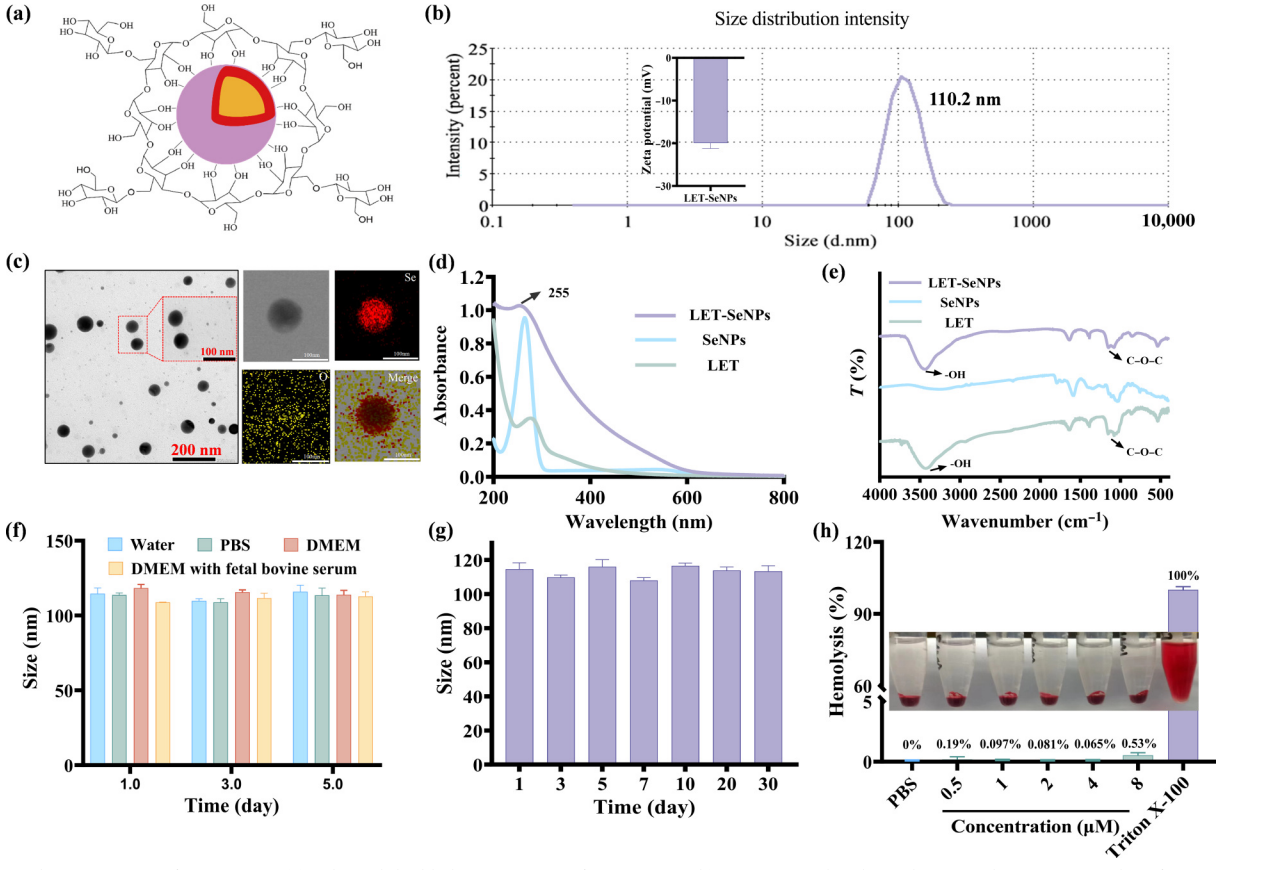

Figure 1 Characterization of LET-SeNPs. (a) Spherical double-layer structure of LET-SeNPs. (b) Zeta potential and size determined using DLS analysis for LET-SeNPs. (c) TEM imaging and elemental analysis mapping images of synthesized LET-SeNPs. (d) Absorption of LET-SeNP UV–vis spectra. (e) LET-SeNP FTIR spectra. (f) LET-SeNP size was stable in different solvents. (g) LET-SeNP size was stable in water for 30 days. (h) Hemolysis of erythrocytes after treatment with different LET-SeNP concentrations.

(TEM) imaging showed that the morphology of LET-SeNPs was monodisperse and exhibited a uniform spherical structure (52.2 ± 10.0 nm in size) (Fig. 1(c)). A characteristic absorption peak of SeNPs at 255 nm was observed in the UV–vis absorption spectra of LET-SeNPs, indicating that SeNPs were present in the synthesized nanoparticles (Fig. 1(d)). Additionally, peaks observed at 1120, 1390, 1630, and 3340 cm^{-1} by Fourier transform infrared spectroscopy (FTIR) indicated the -O- and -OH groups of LET, confirming that the SeNPs were coated with LET (Fig. 1(e)). The synthesized LET-SeNPs maintained a stable particle size for approximately a week in different solvents (PBS, DMEM, and DMEM with fetal bovine serum) while maintaining an average particle size of 110 nm in water at 4 °C for up to one month (Figs. 1(f) and 1(g)). Finally, we evaluated the blood compatibility of the LET-SeNPs. The hemolysis rate of the LET-SeNPs at various concentrations was below 5% compared with that observed in the untreated control group, indicating that the LET-SeNPs did not induce hemolysis when cultured with human blood and had no obvious damage to red blood cells, demonstrating good blood compatibility (Fig. 1(h)). Collectively, these results indicated that the as-synthesized LET-SeNPs were successfully prepared with good stability and biocompatibility.

2.2 Characterization of rBMSCs and the effects of LET-SeNPs on cell proliferation

We conducted *in vitro* experiments with rBMSCs, which share differentiation potential and similar biological characteristics with calvarial suture stem cells [33]. rBMSC extraction is straightforward and relatively easy, rendering rBMSCs ideal for simulating the MPS environment *in vitro*. Primary rBMSCs had a short spindle shape and a relatively large volume (Fig. S5(a) in the Electronic Supplementary Material (ESM)). rBMSCs grew rapidly after subculturing to the third generation. Under the microscope, most cells were spindle-shaped, whereas some were polygonal and closely arranged in vortex-like or radial patterns (Fig. S5(b) in the ESM). Using crystal violet staining (Fig. S6 in the ESM), the nuclei of the rBMSCs were stained dark purple. Alkaline phosphatase (ALP) (Fig. S7(a) in the ESM), Alizarin Red S (ARS)(Fig. S7(b) in the ESM), and Oil Red O staining (Fig. S8 in the ESM) revealed that rBMSCs could differentiate into osteoblasts and adipocytes *in vitro*, expressing alkaline phosphatase activity and forming calcium nodules or lipid droplets. These results indicate that the rBMSCs extracted in this study possess multidirectional stem cell differentiation potential.

We evaluated the biocompatibility of LET-SeNPs on rBMSCs using a cell counting kit-8 (CCK-8) assay (Fig. 2(a)). At 12 and 48 h, all LET-SeNP concentrations promoted cell proliferation ($P < 0.01$). At 24 h, 4 μM LET-SeNPs could promote cell proliferation ($P < 0.05$). As indicated by these results, LET-SeNPs significantly increased rBMSC activity. Although 4 and 8 μM promoted cell proliferation at 12 and 48 h, only 4 μM consistently achieved statistical significance across all three time points, including 24 h, suggesting a superiorly stable dose-response at this concentration.

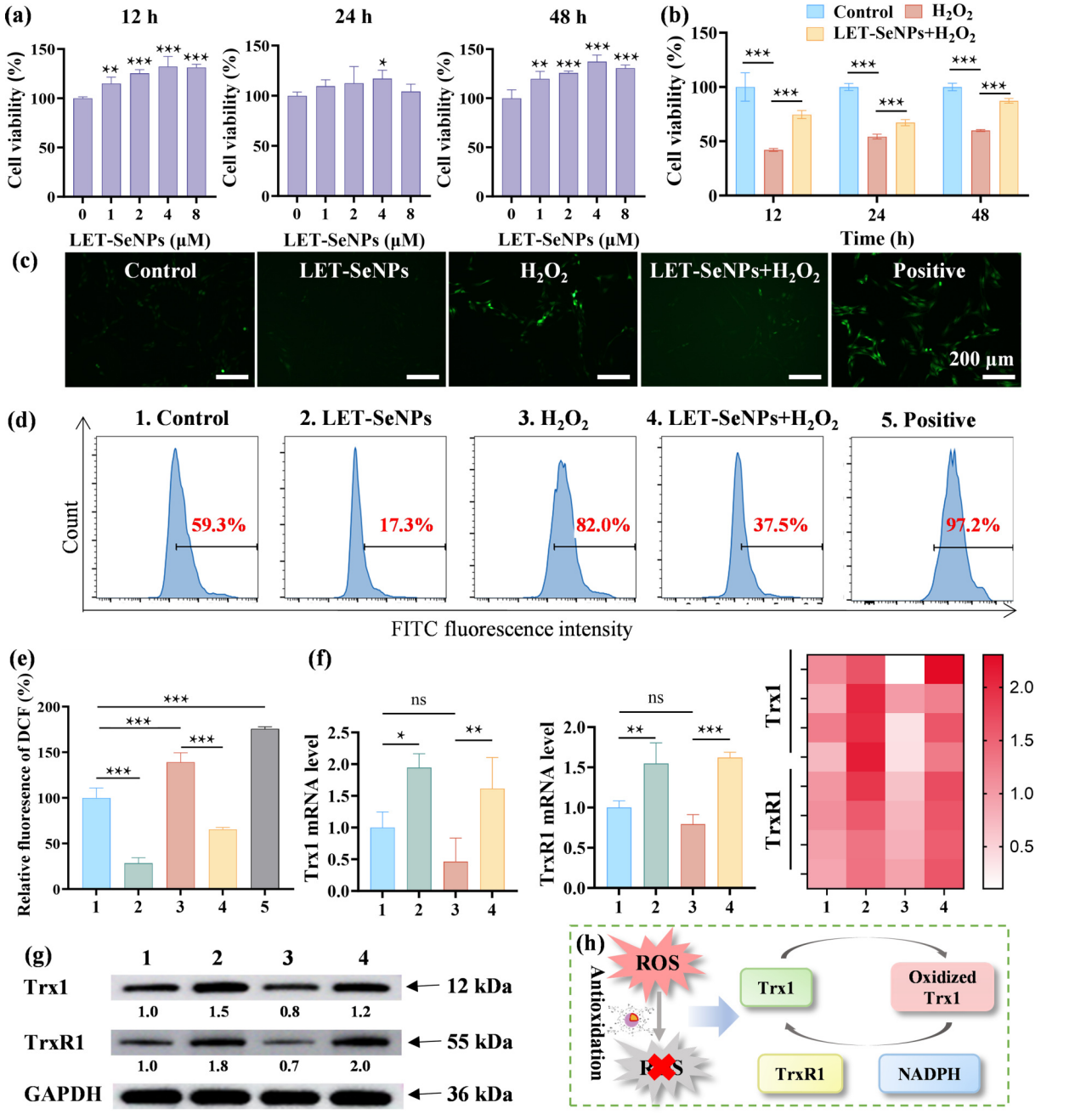

Figure 2 Effects of LET-SeNPs on cell proliferation and cellular ROS content. (a) Effects of LET-SeNPs on rBMSC activity. (b) Inhibitory effect of LET-SeNP pretreatment on H_2O_2-induced oxidative damage of rBMSCs. (c) ROS probe staining. (d) DCF-positive rates detected by flow cytometry. (e) Histogram of DCF-positive rates in each group. (f) Measurement of *Trx1* and *TrxR1* expression levels by qRT-PCR. (g) Measurement of Trx1 and TrxR1 protein expression levels by western blotting. (h) Diagram of LET-SeNPs eliminating ROS during osteogenesis via the Trx1/TrxR1 system. Data are presented as the mean ± standard deviation, $n = 4$; *significant difference compared with the control group, ns: not significant, $^*P < 0.05$, $^{**}P < 0.01$, $^{***}P < 0.001$.

Therefore, 4 μM was selected for all subsequent experiments as the optimal working concentration. H_2O_2 was employed as an inducer of OS as it is the primary source of ROS generated within cells. Being a neutral, non-free radical molecule, it is relatively stable [34] and is commonly used to simulate the OS environment *in vitro*. After the addition of H_2O_2, rBMSC activity decreased significantly ($P < 0.001$); however, it increased significantly after pretreatment with LET-SeNPs ($P < 0.001$) (Fig. 2(b)), indicating that LET-SeNPs provided strong antioxidant properties, protected cells, and maintained viability under OS conditions.

2.3 LET-SeNPs reduced intracellular rBMSC ROS levels via the Trx1/TrxR1 system

DCFH-DA was used as a probe to detect cellular ROS levels in each group. Once 2',7'-dichlorodihydrofluorescein diacetate (DCFH-DA) enters the cell membrane, it is hydrolyzed into nonfluorescent DCFH, which is subsequently oxidized by ROS within the cells to generate fluorescent 2',7'-dichlorofluorescein (DCF). DCF fluorescence was measured to assess ROS levels in the cells. DCFH-DA fluorescent probe staining (Fig. 2(c)) showed that rBMSCs in the positive control and H_2O_2 groups emitted green fluorescence,

whereas only a few cells in the control, LET-SeNPs, and LET-SeNPs + H_2O_2 groups were labeled with DCF. Flow cytometry (Figs. 2(d) and 2(e), and Fig. S9 in the ESM) showed that the proportion of DCF-positive cells was lower in the LET-SeNPs group than in the control group ($P < 0.001$). Furthermore, the LET-SeNPs + H_2O_2 group showed a reduced percentage of DCF-positive cells relative to the H_2O_2 group ($P < 0.001$). Treatment with LET-SeNPs decreased intracellular ROS levels in rBMSCs.

The thioredoxin (Trx) system, comprising thioredoxin, thioredoxin reductase (TrxR), and reduced nicotinamide adenine dinucleotide phosphate, is a major enzymatic system for regulating ROS levels; it constitutes an important antioxidant defense system in the body [35]. Studies have shown that SeNPs inhibit ROS and inflammatory factors via TrxR1, thereby remodeling the microenvironment and activating downstream pathways to enhance osteogenic processes and accelerate bone repair [36–38]. Therefore, we examined *TrxR1* and *Trx1* expression levels in LET-SeNP-treated cells. RT-qPCR (Fig. 2(f)) revealed that during the initial stage of osteogenic induction, compared with the control group, the LET-SeNPs group exhibited increased *Trx1* and *TrxR1* mRNA expression levels ($P < 0.05$). Compared with the H_2O_2 group, the LET-SeNPs + H_2O_2 group exhibited elevated *Trx1* and *TrxR1* mRNA expression levels ($P < 0.05$). As shown in Fig. 2(g), Trx1 and TrxR1 protein expression levels were significantly elevated in the LET-SeNPs and LET-SeNPs + H_2O_2 groups compared with those in the control and H_2O_2 groups ($P < 0.05$), respectively, consistent with the mRNA expression data. These results indicate that LET-SeNPs eliminate ROS and inhibit OS during osteogenesis via the Trx1/TrxR1 system (Fig. 2(h)).

2.4 LET-SeNPs mitigated the decreased osteogenic differentiation potential of rBMSCs caused by oxidative damage

To assess the impact of LET-SeNPs on oxidative damage suppression and osteogenesis promotion, we performed ALP staining, ARS staining, and the corresponding quantitative analyses. ALP staining (Fig. 3(a)) showed that the control and LET-SeNPs groups presented distinct blue-purple staining, with deeper staining in the LET-SeNPs group than in the control group. The H_2O_2 group was almost colorless, whereas the LET-SeNPs + H_2O_2 group was prominently stained. Quantitative analysis (Fig. 3(b)) also revealed that ALP activity was significantly higher in the LET-SeNPs group than in the control group ($P < 0.001$), whereas the H_2O_2 group exhibited a significant decrease in ALP activity ($P < 0.001$). Additionally, the LET-SeNPs + H_2O_2 group showed

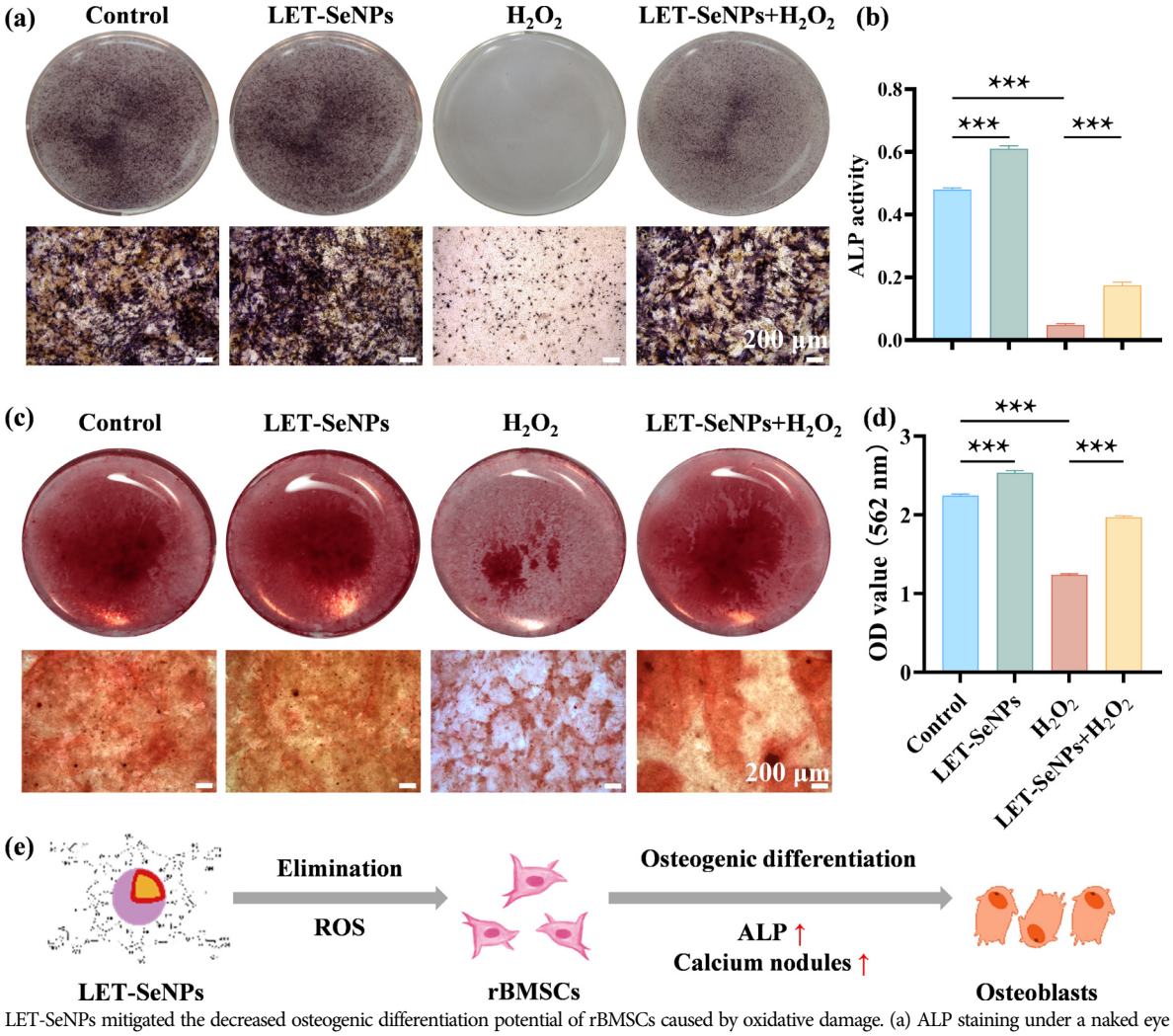

Figure 3 LET-SeNPs mitigated the decreased osteogenic differentiation potential of rBMSCs caused by oxidative damage. (a) ALP staining under a naked eye and light microscope. (b) Quantitative analysis of ALP activity. (c) ARS staining under a naked eye and light microscope. (d) Quantitative analysis of ARS staining. (e) Diagram of LET-SeNPs promoting osteogenic differentiation of rBMSCs. Data are presented as the mean ± standard deviation, $n = 3$; ***$P < 0.001$.

significantly higher ALP activity than the H_2O_2 group ($P < 0.001$). ARS staining showed similar trends (Fig. 3(c)). The LET-SeNPs group demonstrated more intense red staining and more mineralized nodules than the control group (Fig. 3(d)) ($P < 0.001$), whereas the H_2O_2 group displayed lighter staining and significantly fewer mineralized nodules ($P < 0.001$). Compared with the H_2O_2 group, the LET-SeNPs + H_2O_2 group exhibited a significantly higher content of mineralized nodules ($P < 0.001$). These results suggest that LET-SeNPs alleviate the decline in osteogenic differentiation potential of rBMSCs caused by oxidative damage (Fig. 3(e)).

2.5 LET-SeNPs potentiated bone regeneration in a rat MPS model

To evaluate the effect of LET-SeNPs on bone regeneration, we used the maxillary anterior tooth expansion method to establish a rat RME model (Fig. 4(a)). A self-activating expander with an adjustable expansion force was developed for this purpose. This expander comprised a helical spring and bilateral expansion arms that included force adjustment angles (Fig. S3 in the ESM). During expansion, the expander contacted the incisors and exerted an indirect expansion force on the maxilla through their roots. After 7 days of expansion, the distance between the incisors significantly increased. Subsequently, the helical spring was bonded to a light-curing resin to deactivate the expander and convert it into a retainer. During 4 days of continuous wear of the expanders and retainers, the distance between the incisors did not show any significant differences between the groups ($P > 0.05$); the distance between the incisors in both groups gradually increased after the establishment of the RME model (Fig. 4(b)). The incisors expanded by more than 3 mm within 7 days (approximately 0.42 mm/day). The measured values did not show any significant differences between days 7 and 14 ($P > 0.05$), indicating that the retention was effective. In the initial 2 days of maxillary expansion, rats in the RME and LET-SeNPs groups showed a reduction in body weight. However, starting on day 3, their body weight started to rise (Fig. S10 in the ESM). None of the rats exhibited diarrhea or other gastrointestinal symptoms. No statistically significant differences were noted in average body weight between the groups throughout the experiment ($P > 0.05$).

To minimize potential systemic effects associated with

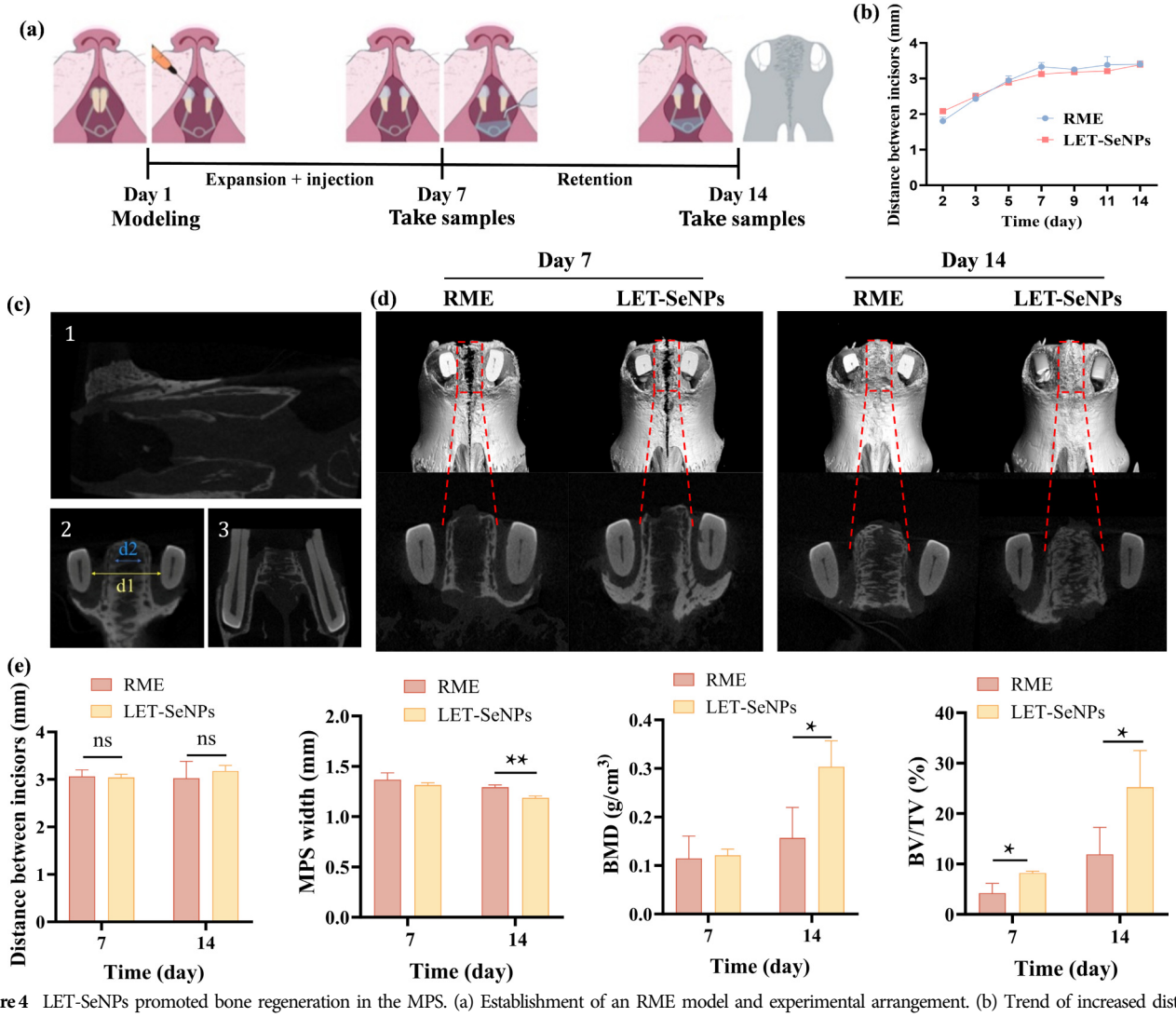

Figure 4 LET-SeNPs promoted bone regeneration in the MPS. (a) Establishment of an RME model and experimental arrangement. (b) Trend of increased distance between incisors. (c) Micro-CT 3D reconstruction of a rat maxilla. 1: sagittal direction; 2: coronal direction; 3: horizontal direction; d1: distance between incisors; d2: MPS width. (d) Micro-CT 3D reconstruction of MPS. (e) Quantitative analysis of the distance between incisors, MPS width, BMD, and BV/TV. Data are presented as the mean ± standard deviation, $n = 3$; *significant difference compared with the control group, ns: not significant, $^*P < 0.05$, $^{**}P < 0.01$.

pleiotropic actions of SeNPs, local injection was chosen as the preferred administration route. Additionally, considering the development of new tissue in MPS after day 7, continuous injections may potentially cause physical damage to the tissue. Therefore, the injection regimen was started on day 1 and administered every other day to MPS, stopping on day 7. To ascertain the sustained impact of LET-SeNP injection and its discontinuation on suture remodeling, micro-computed tomography (micro-CT) 3D reconstruction of the rat maxilla in various directions was conducted on days 7 and 14 (Fig. 4(c)). The anatomical structure of the rat maxilla MPS was clearly observed in the images (Fig. 4(d)). The distance between the incisors (d1) and MPS width (d2) were measured using 3DMed. On day 7, the LET-SeNPs and RME groups showed significant increases in incisor distance and MPS width; however, no significant differences were observed between the groups ($P > 0.05$) (Figs. 4(d) and 4(e)). By day 14, there was still no significant difference in incisor distance between the groups ($P > 0.05$). The MPS gap was filled with bone tissue (Figs. 4(d) and 4(e)); the LET-SeNPs group had a smaller gap than the control group. The LET-SeNPs group showed significantly higher bone volume/tissue volume (BV/TV) values than the control group on days 7 and 14 ($P < 0.05$). By day 14, bone mineral density (BMD) was significantly higher in the LET-SeNPs group than in the control group ($P < 0.05$). These results indicated that our RME model was effective and that local injection of LET-SeNPs could potentiate bone formation in MPS.

2.6 LET-SeNPs accelerated new bone maturation in MPS

Tissue sections of the rat maxilla were observed to analyze new bone maturation in MPS with LET-SeNPs treatment. Hematoxylin and eosin (H&E) staining (Fig. 5(a) and Fig. S11 in the ESM) distinctly showed the structure of the maxillary palatine suture area; five layers of the anterior palatine area were discernible from left to right: the left maxillary palatine plate, fiber insertion layer, intermediate layer (abundant in fibers and mesenchyme), right fiber insertion layer, and right maxillary palatine plate. Over time, the expanded bone suture was gradually filled with new bone tissue; protrusions on both sides extended and grew toward the intermediate layer, leading to a gradual reduction in its width. Considerable aggregation of osteoblasts and the formation of new capillaries were observed. On day 14, the intermediate layer width was smaller in the LET-SeNPs group than in the control group, suggesting that treatment with LET-SeNPs effectively accelerated MPS healing.

Using Masson's trichrome staining, mineralized collagen and mature bone matrix were stained red, whereas non-mineralized collagen and immature bone matrix were stained blue. Seven days after expansion, the intermediate layer of MPS was almost entirely composed of collagen fibers (light blue area), with a blue-stained immature bone matrix on both sides of the intermediate layer and a red-stained mature bone matrix in the bone tissue (Fig. 5(b) and Fig. S11 in the ESM). On day 14, bone tissue was interspersed within the intermediate layer; there was an increased amount of mature bone matrix. Furthermore, we performed a quantitative analysis of the optical density values in these images to evaluate the areas of non-osseous gaps, mature bone, and relative mature bone ratio (area of mature bone/area of non-osseous gaps). On days 7 and 14, the area of non-osseous gaps was larger in the RME group than in the LET-SeNPs group ($P < 0.01$) (Fig. 5(c)), whereas the area of mature bone was smaller in the RME group than in the LET-SeNPs group ($P < 0.01$). Similarly, the relative mature bone ratio was higher in the LET-SeNPs group than in the RME group ($P < 0.01$). These results demonstrated that LET-SeNPs significantly accelerated new bone maturation in MPS.

2.7 LET-SeNPs accelerated bone regeneration by promoting osteoblastogenesis and inhibiting osteoclast expression

Osteoblast activity was measured using osteocalcin (OCN), which is located in the cytoplasm of osteoblasts and periosteum cells. Anti-OCN antibody staining showed (Fig. 6(a)) that OCN-positive cells were observed on bilateral palatine bone surfaces along the margins of new bones and clustered in sutures to a greater extent in the LET-SeNPs group than in the RME group. Optical density value analysis of the images (Fig. 6(b)) revealed that on days 7 and 14, the LET-SeNPs group exhibited a significantly larger proportion of OCN-positive stained areas ($P < 0.01$) than the RME group. According to tartrate- resistant acid phosphatase (TRAP) staining (Fig. 6(c)), osteoclasts with red cytoplasm were mostly distributed along the trabecular border; a small amount was distributed in non-bony fibrous tissues. Quantitative analysis revealed that the RME group had a higher number of osteoclasts than the LET-SeNPs group on days 7 and 14 ($P < 0.05$) (Fig. 6(d)). A reduction in osteoclast number and activity can lead to increased bone mass and strength [39–42]. These results suggest that LET-SeNPs accelerate bone regeneration by promoting mesenchymal stem cell differentiation into osteoblasts in MPS and inhibiting osteoclastogenesis (Fig. 6(e)).

3 Conclusions

In summary, the results of this study demonstrate that the use of LET-SeNPs is a novel and effective strategy for enhancing bone remodeling in MPS following RME. Our findings revealed that LET-SeNPs enhanced the proliferative and osteogenic capacity of rBMSCs and mitigated OS via the Trx1/TrxR1 system, further improving their antioxidant defense mechanisms. *In vivo* experiments confirmed that local administration of LET-SeNPs significantly accelerated MPS bone formation by stimulating osteoblast activity while suppressing osteoclast-mediated bone resorption. These results highlight the therapeutic potential of LET-SeNPs in optimizing RME outcomes by preventing relapse due to insufficient bone remodeling. Further clinical studies are warranted to validate the translational applicability of this approach in orthodontic practice.

4 Experimental

4.1 Materials

The CCK-8 reagent was purchased from Dojindo. An ALP assay kit was purchased from Nanjing Jiancheng Bioengineering Institute. Radioimmunoprecipitation assay (RIPA) lysis buffer and a 5-bromo-4-chloro-3-indolyl phosphate/nitro blue tetrazolium (BCIP/NBT) kit were purchased from Beyotime. A bicinchoninic acid (BCA) protein assay kit and cetylpyridinium chloride were purchased from Coolaber. Osteogenic and adipogenic induction media were purchased from OriCell. ARS solution was purchased from Solarbio.

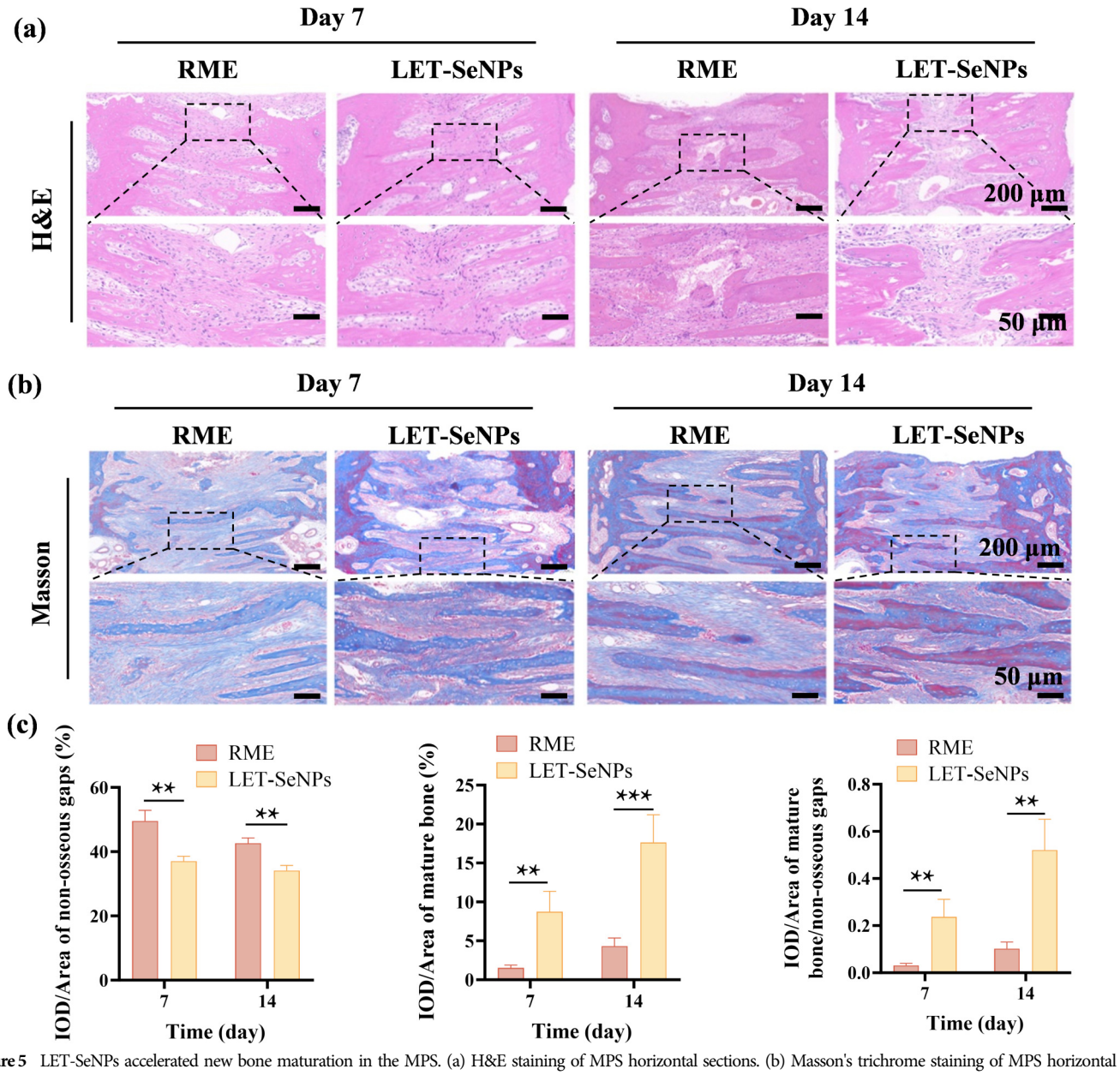

Figure 5 LET-SeNPs accelerated new bone maturation in the MPS. (a) H&E staining of MPS horizontal sections. (b) Masson's trichrome staining of MPS horizontal sections. (c) Quantitative analysis of Masson's trichrome staining. Data are presented as the mean ± standard deviation, $n = 3$; *significant difference compared with the control group, $^{**}P < 0.01$, $^{***}P < 0.001$.

4.2 Preparation and characterization of LET-SeNPs

LET-SeNPs were synthesized according to a previously described procedure. Briefly, 3 mL of 50 mM sodium selenite (Na_2SeO_3) solution was combined with 6 mL of 10 mg/mL LET solution under gentle stirring. Next, 3 mL of 200 mM vitamin C (Vc) solution was added dropwise to the mixture; the total volume was adjusted to 30 mL using Milli-Q water. The reaction mixture was magnetically stirred at room temperature for 12 h, which was followed by dialysis in Milli-Q water for 24 h to remove unreacted Na_2SeO_3 and Vc. The resulting LET-SeNPs were stored at 4 °C until further use.

The hydrodynamic size and surface charge of LET-SeNPs were determined by DLS and zeta potential analysis, respectively. Their structural characteristics were analyzed using UV–vis spectrometry; their functional groups were identified using FTIR. TEM was used to visualize the nanoparticle morphology. Se content in the LET-SeNPs was quantified using inductively coupled plasma mass spectrometry. Additionally, the stability of the nanoparticles in water was assessed by measuring their size using DLS.

4.3 CCK-8 assay

Once rBMSCs adhered to the 96-well plates (2×10^3 cells/well), they were cultivated in a complete medium (containing 0, 1, 2, 4, 8 μM of LET-SeNPs) for 12, 24, and 48 h. Subsequently, the CCK-8 reagent was replaced. Optical density values at 450 nm were measured using a microplate reader (Bio-Rad, iMark™ microplate absorptiometer, California, USA) after incubation at 37 °C for 2.5–3 h.

Subsequently, the inhibitory effect of LET-SeNP pretreatment on H_2O_2-induced oxidative damage was evaluated. The rBMSCs were classified into three groups: A (control), B (H_2O_2), and C (LET-

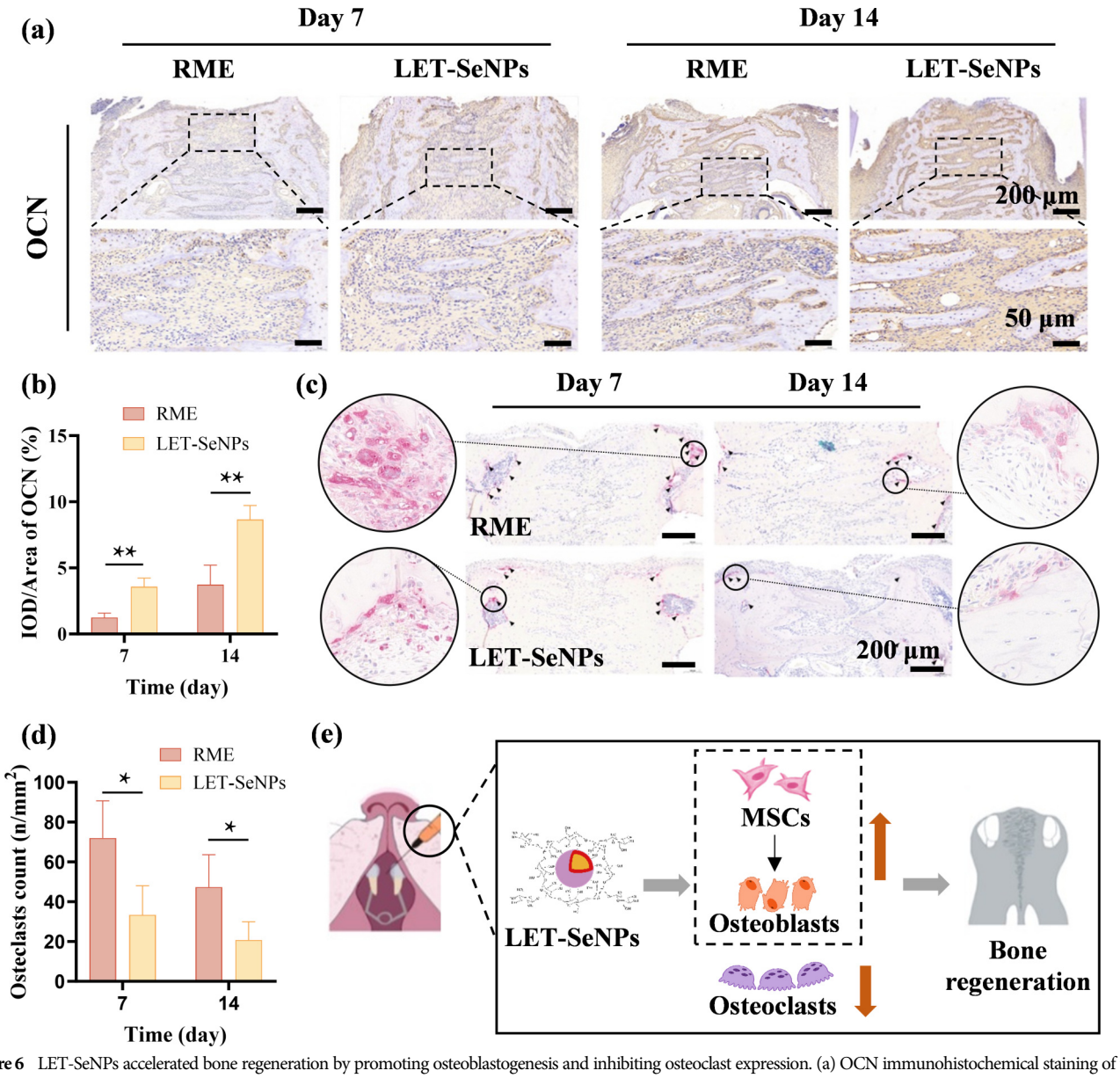

Figure 6 LET-SeNPs accelerated bone regeneration by promoting osteoblastogenesis and inhibiting osteoclast expression. (a) OCN immunohistochemical staining of the MPS horizontal sections. (b) Quantitative analysis of immunohistochemical staining. (c) TRAP staining of MPS horizontal sections. Black arrows indicate osteoclasts. (d) Quantitative analysis of TRAP staining. (e) Diagram of LET-SeNPs promoting osteoblast generation and inhibiting osteoclastogenesis. Data are presented as the mean ± standard deviation, $n = 3$; *significant difference compared with the control group, $^{*}P < 0.05$, $^{**}P < 0.01$.

SeNPs + H_2O_2). After 24 h of culture, the media in groups A and B were replaced with complete media, whereas that in group C was replaced with a complete medium containing 4 μM LET-SeNPs. After 12, 24, and 48 h, 100 μM H_2O_2 was added to each group. After an additional 24 h of culture, the CCK-8 reagent was replaced; the absorbance was determined at 450 nm after incubation.

4.4 Cellular ROS detection assay

Cells were plated in six-well plates (4×10^4 cells/well) and divided into five groups: A (positive control), B (control), C (LET-SeNPs), D (H_2O_2), and E (LET-SeNPs + H_2O_2). Culture media were replaced in groups A, B, and D, whereas those containing 4 μM LET-SeNPs were replaced in groups C and E. After 24 h, H_2O_2 was added to groups D and E to obtain culture media containing 100 μM H_2O_2. After another 24 h, the culture media were aspirated from all groups; the cells were rinsed twice with PBS. Next, DCFH-DA solution was added and mixed thoroughly. Additionally, 2 μL of Rosup-positive inducer was added to group A. After a 20-min incubation at 37 °C, the cells were washed twice with a serum-free culture medium to completely remove any unincorporated DCFH-DA. Fluorescence intensity was examined using an inverted fluorescence microscope.

For flow cytometry assay, groups A–E were cultivated under the same conditions as described above; an additional group, F (negative control), was established, in which no cells were inoculated. The cell suspension was centrifuged at 1000 rpm for 5 min, after which the supernatant was removed. DCFH-DA working solution was added and thoroughly mixed. Rosup-positive inducer was added to group A. Incubation was carried out with gentle inversion and mixing every 3–5 min. The cells were washed twice with a serum-free culture medium and centrifuged to remove the supernatants. The cells were resuspended in PBS and

transferred to 96-well plates. A flow cytometer was used to set parameters of the fluorescein isothiocyanate (FITC) channel to detect the DCF-positive rate.

4.5 Quantitative real-time PCR

Cells were inoculated in six-well plates (2×10^5 cells/well) and assigned to four groups: A (control), B (LET-SeNPs), C (H_2O_2), and D (LET-SeNPs + H_2O_2). After 24 h, complete media were replaced in groups A and C, whereas complete media containing 4 μM LET-SeNPs were replaced in groups B and D. After 24 h of culture, H_2O_2 was added to groups C and D. After another 24 h, the media were replaced with osteogenic induction media.

A day after osteogenic induction, total RNA was extracted; its concentration was measured. Complementary DNA was synthesized via reverse transcription. A 10 μL reaction system was employed; the primers were commercially synthesized (Sangon, Shanghai, China), and their sequences are listed in Table S1 in the ESM. Glyceraldehyde-3-phosphate dehydrogenase was utilized as the internal reference gene; *Trx1* and *TrxR1* mRNA expression levels were quantified using the $2^{-\Delta\Delta Ct}$ method to assess their expression.

4.6 ALP staining and ALP activity assay

Cell inoculation, grouping, and culturing methods were consistent with those used for qRT-PCR. ALP staining was conducted using a BCIP/NBT kit 7 days after osteogenic induction.

ALP activity was determined using an ALP assay kit. After 7 days of osteogenic induction, RIPA lysis buffer was added; the cells were lysed on ice for 1 h. Cell lysates were collected using cell scrapers and centrifuged at 12,000 rpm for 15 min at 4 °C. The supernatant absorbance was measured at 595 nm. A BCA protein assay kit was used to determine the protein concentration in each group. The samples, buffer, and substrate solution were added to 96-well plates, which were subsequently incubated in a 37 °C water bath for 15 min. Subsequently, a chromogenic reagent was added; the absorbance was measured at 520 nm. ALP levels in each group were calculated.

4.7 ARS staining

Cell inoculation, grouping, and culturing methods were consistent with those used for qRT-PCR. After 21 days of osteogenic induction, cells were stained with ARS. The stained plates were examined under an inverted microscope to assess calcium nodule formation. Next, 10% cetylpyridinium chloride was added for quantitative analysis. After 1 h of incubation, the absorbance of the eluted solution was measured at 562 nm.

4.8 RME model

Six-week-old male Sprague-Dawley rats with complete incisors were used for modeling. Each rat was first administered general anesthesia via an intraperitoneal injection of 3% pentobarbital sodium; the upper and lower jaws of the rat were subsequently opened and fixed. Before placing the expander, a low-speed dental phone was used to drill a small circular gap at the gingival edge near the incisors to allow the expander to be inserted between them. The incisors were wiped, acid-etched for 30 s, rinsed, blown dry, and photocured with an adhesive for 10 s. The expander was placed such that the arm end was bent and wound around each incisor through the gap; the spiral spring was pressed tightly on the palatal papilla. The expander was subsequently molded into the buccal and distal surfaces using a light-curing fluid resin cement. It was glued to the incisor and photocured for 30 s. On day 7, the expanders were converted into retainers. Subsequently, on days 7 and 14, the rats were euthanized via intraperitoneal injection of an excessive dose of 3% pentobarbital sodium. Rat maxillae were dissected using scissors and tissue forceps; all soft tissues were removed. After removing the light-cured resin and expander/retainer, the maxillae were rinsed with physiological saline and placed in centrifuge tubes containing 4% paraformaldehyde for tissue fixation. The Laboratory Animal Welfare and Ethics Committee of Jinan University approved all animal experimental procedures (ethical code: 20220906-3).

4.9 Research design

In total, 24 rats were randomly assigned to the RME and LET-SeNPs groups (n = 12 per group). After modeling, LET-SeNP solutions (40 μg/kg, 0.1 mL per injection using a 1 mL syringe) were injected locally into MPS on days 1, 3, 5, and 7 of the experiment, delivering an Se dose of approximately 8.8 μg per session and a cumulative dose of approximately 35.2 μg per rat; 6 rats from both groups were sacrificed on days 7 and 14, respectively (Fig. 4(a) and Fig. S2 in the ESM). Using H&E staining, Masson's trichrome staining, OCN immunohistochemical staining, TRAP staining, and quantitative analysis of micro-CT three-dimensional (3D) reconstruction, the histological and morphological changes of MPS in different groups on days 7 and 14 were observed to evaluate the effect of local injection of LET-SeNPs on new bone formation.

4.10 Design of the expander and retainer

The expander was constructed using 0.014-inch stainless steel wire, which was shaped into a helical spring (ϕ2 mm); expansion force was provided by expander arms at the bilateral curved ends (Fig. S3 in the ESM). Expansion force was regulated by adjusting the bending angle of the expander arms. A dynamometer was used to calibrate force when closing the expander arms of each expander to 100 g, with an error range of ±5 g. A light-cured flow resin cement was employed to wrap the range from the helical spring to the bending angle to deactivate the expander, eliminate elastic strain, and transform it into a retainer that remained *in situ*.

4.11 Measurement of distance between incisors

On days 2, 3, 5, 7, 9, 11, and 14 after model establishment, the distance between the maxillary incisors at the gingival level was measured using Vernier calipers (Fig. S4 in the ESM). Measurements were conducted separately for three individuals; the average value was obtained after each measurement.

4.12 Micro-CT analysis

After the rats were sacrificed, their maxillae were fixed in 4% paraformaldehyde for 24 h. Micro-CT was used to scan the specimens and quantify BMD and BV/TV. The region of interest (ROI) was defined as a standardized rectangular volume (1.05 mm × 1.5 mm × 0.9 mm) centered on MPS between two maxillary incisors, with boundaries delineated using consistent anatomical landmarks, specifically the palatal papilla and anterior palatine suture. The same ROI was uniformly applied across all specimens at both time points (days 7 and 14) to ensure comparability between the groups. Quantitative analysis of BMD and BV/TV within the defined ROI was performed using 3DMed.

4.13 Tissue staining

Rat maxillae were immersed in 10% EDTA for decalcification after fixation. The decalcifying solution was changed weekly; the entire process took approximately four weeks to complete. Once decalcification was achieved, continuous tissue sections (5 μm thick) were prepared using the paraffin embedding technique, which was oriented horizontally. H&E staining was performed to examine new bone formation. Integrated optical densities of the red and blue regions in Masson's trichrome staining were analyzed. For OCN immunohistochemical staining, tissue sections were incubated with primary antibodies overnight at 4 °C, which was followed by a 2-h incubation at room temperature with horseradish peroxidase-conjugated goat anti-rabbit secondary antibodies. The sections were stained with hematoxylin and sealed. TRAP staining was performed to assess osteoclast content and distribution.

4.14 Statistical analysis

Experimental results are presented as the mean ± standard deviation. Student's *t*-test was used for comparisons between two groups. When assessing three or more groups, one-way ANOVA with a completely randomized design was used. $P < 0.05$ was considered statistically significant. Statistical charts were created using GraphPad Prism 10.1.2.

Electronic Supplementary Material: Supplementary material (details of isolation, cultivation and detection of rBMSCs, steps for establishing the Sprague-Dawley rat RME model, the weight change trend of rats after modeling, and primer sequences for qRT-PCR) is available in the online version of this article at https://doi.org/10.26599/NR.2026.94908704.

Data availability

All data needed to support the conclusions in the paper are presented in the manuscript and/or the Electronic Supplementary Material. Additional data related to this paper may be requested from the corresponding author upon request.

Acknowledgements

This study was supported by the National Natural Science Foundation of China (No. 82370995), Fundamental and Interdisciplinary Disciplines Breakthrough Plan of the Ministry of Education of China (No. JYB2025XDXM802), Guangzhou Key Research and Development Program (No. 2025B03J0143), Guangzhou Basic and Applied Basic Research Foundation (No. 2025A04J5183), and Youth S&T Talent Support Programme of Guangdong Provincial Association for Science and Technology (No. SKXRC2025324).

Declaration of competing interest

All the contributing authors report no conflict of interests in this work.

Author contribution statement

Y. L. and T. L.: Data curation, project administration, validation, writing manuscript, experimental design. U. M. C., Y. Z. X., R. D., and X. W.: Data curation, project administration, validation, experimental design. Q. F.: Project administration, writing manuscript. T. F. C. and Y. H.: Project administration, funding acquisition, writing manuscript. All the authors have approved the final manuscript.

Informed consent

Not applicable.

Ethics statement

The animal experiments were carried out following the guidelines of the Laboratory Animal Welfare and Ethics Committee of Jinan University for the Care and Use of Laboratory Animals and were approved by the Laboratory Animal Welfare and Ethics Committee of Jinan University (Ethical code: 20220906-3).

Use of AI statement

None.

References

[1] McNamaraa, J. A. Maxillary transverse deficiency. *Am. J. Orthod. Dentofac. Orthop.* **2000**, *117*, 567–570.
[2] Chen, Y. W.; He, H. Advances in diagnostic methods of maxillary transverse deficiency. *Chin. J. Stomatol.* **2021**, *56*, 104–108.
[3] Sakai, R. H. U. S.; de Assumpção, M. S.; Ribeiro, J. D.; Sakano, E. Impact of rapid maxillary expansion on mouth-breathing children and adolescents: A systematic review. *J. Clin. Exp. Dent.* **2021**, *13*, e1258–e1270.
[4] Baccetti, T.; Franchi, L.; Cameron, C. G.; McNamara, J. A. Jr. Treatment timing for rapid maxillary expansion. *Angle Orthod.* **2001**, *71*, 343–350.
[5] Liu, S. Y.; Xu, T. M.; Zou, W. Effects of rapid maxillary expansion on the midpalatal suture: A systematic review. *Eur. J. Orthod.* **2015**, *37*, 651–655.
[6] Braun, S.; Bottrel, J. A.; Lee, K. G.; Lunazzi, J. J.; Legan, H. L. The biomechanics of rapid maxillary sutural expansion. *Am. J. Orthod. Dentofac. Orthop.* **2000**, *118*, 257–261.
[7] Koca, C. G.; Sadry, S.; Asker, H.; Çiçek, M. F.; Kösehasanoğulları, M.; Kaya, G. Effects of the different administration frequencies of teriparatide (PTH [1-34]) on new bone formation of expanded midpalatal sutures in rats: A histomorphometric and micro-computed tomography analysis. *Orthod. Craniofac. Res.* **2021**, *24*, 449–457.
[8] Wang, F.; Qian, H. J.; Kong, L. C.; Wang, W. B.; Wang, X. Y.; Xu, Z.; Chai, Y. M.; Xu, J.; Kang, Q. L. Accelerated bone regeneration by astragaloside IV through stimulating the coupling of osteogenesis and angiogenesis. *Int. J. Biol. Sci.* **2021**, *17*, 1821–1836.
[9] Pirmoradian, M.; Safiaghdam, H.; Nokhbatolfoghahaei, H.; Ashnagar, S.; Fekrazad, R. Effect of photobiomodulation on relapse in an experimental rapid maxillary expansion model in rat. *Photochem. Photobiol.* **2021**, *97*, 634–640.
[10] Zhao, H. J.; Wang, X. Y.; Jin, A. T.; Wang, M. J.; Wang, Z. Y.; Huang, X. T.; Dai, J. W.; Wang, X. D.; Lin, D.; Shen, S. G. Reducing relapse and accelerating osteogenesis in rapid maxillary expansion using an injectable mesoporous bioactive glass/fibrin glue composite hydrogel. *Bioact. Mater.* **2022**, *18*, 507–525.
[11] Simsek, D.; Gok, G. D.; Delipinar, S. D. Does krill oil enhancing the new bone formation in orthopedically expanded median palatal suture in rat model? A micro-CT and immunohistochemical analysis. *BMC Oral Health* **2024**, *24*, 862.
[12] Vali, S.; Khosravani, S.; Nobar, B. R.; Motamedian, S. R. Rapid maxillary expansion supplementary methods: A scoping review of animal studies. *Int. Orthod.* **2022**, *20*, 100614.
[13] Lv, N.; Sun, H. F.; Tang, W. X.; Li, Y. G.; Qian, Z. L.; Hong, L. H.;

Chen, C.; Li, H. Y.; Bai, J. X.; Qiao, Y. S. et al. A smart bio-battery facilitates diabetic bone defect repair via inducing macrophage reprogramming and synergistically modulating bone remodeling coupling. *Adv. Funct. Mater.* **2026**, *36*, e15820.

[14] Bai, X. C.; Lu, D.; Bai, J.; Zheng, H.; Ke, Z. Y.; Li, X. M.; Luo, S. Q. Oxidative stress inhibits osteoblastic differentiation of bone cells by ERK and NF-κB. *Biochem. Biophys. Res. Commun.* **2004**, *314*, 197–207.

[15] Ahmad Hairi, H.; Jayusman, P. A.; Shuid, A. N. Revisiting resveratrol as an osteoprotective agent: Molecular evidence from *in vivo* and *in vitro* studies. *Biomedicines* **2023**, *11*, 1453.

[16] Zachara, B. A.; Pawluk, H.; Bloch-Boguslawska, E.; Śliwka, K. M.; Korenkiewicz, J.; Skok, Ź.; Ryć, K. Tissue level, distribution and total body selenium content in healthy and diseased humans in Poland. *Arch. Environ. Health: An Int. J.* **2001**, *56*, 461–466.

[17] Xiong, Z. S.; Lin, H.; Li, H.; Zou, B. H.; Xie, B.; Yu, Y. Z.; He, L. Z.; Chen, T. F. Chiral selenium nanotherapeutics regulates selenoproteins to attenuate glucocorticoid-induced osteoporosis. *Adv. Funct. Mater.* **2023**, *33*, 2212970.

[18] Liu, C.; Wang, C. Q.; Liu, Y.; Huang, J. H.; Xu, W. N.; Li, J. J.; Wang, Y. H.; Xu, Y. Z.; Zhu, L. X.; Xu, H. X. Selenium nanoparticles/carboxymethyl chitosan/alginate antioxidant hydrogel for treating steroid-induced osteonecrosis of the femoral head. *Int. J. Pharm.* **2024**, *653*, 123929.

[19] Zheng, W. Y.; Ma, L.; Luo, X. S.; Xu, R. H.; Cao, Z. Y.; He, Y. N.; Chang, Y. Z.; You, Y. Y.; Chen, T. F.; Liu, H. M. Ultrasound-triggered functional hydrogel promotes multistage bone regeneration. *Biomaterials* **2024**, *311*, 122650.

[20] Liu, J. G.; Mai, L.; Tan, A. W.; Du, Y. X.; Luo, J. Y.; Xu, S. Y.; Rao, S. Y.; Chen, S. H.; Su, G. Y.; Chen, T. F. et al. Self-enhancing drug pair-driven selenium nanotherapeutics reverses microglial pyroptosis through NLRP3/caspase-1 pathway and neuronal apoptosis for treatment of spinal cord injury. *Adv. Funct. Mater.* **2025**, *35*, 2503505.

[21] Xiao, X.; Deng, H.; Lin, X.; Ali, A. S. M.; Viscardi, A.; Guo, Z. W.; Qiao, L. C.; He, Y. J.; Han, J. Selenium nanoparticles: Properties, preparation methods, and therapeutic applications. *Chem.-Biol. Interact.* **2023**, *378*, 110483.

[22] Xu, R. H.; You, Y. Y.; Zheng, W. Y.; Ma, L.; Chang, Y. Z.; Pan, S. Y.; He, Y. N.; Zhou, M. J.; Xu, Z. L.; Chen, T. F. et al. Selenoprotein-regulated hydrogel for ultrasound-controlled microenvironment remodeling to promote bone defect repair. *Adv. Funct. Mater.* **2024**, *34*, 2313122.

[23] Huang, L.; Zhang, S. H.; Bian, M. X.; Xiang, X. D.; Xiao, L.; Wang, J. Y.; Lu, S. Y.; Chen, W.; Zhang, C.; Mo, G. K. et al. Injectable, anti-collapse, adhesive, plastic and bioactive bone graft substitute promotes bone regeneration by moderating oxidative stress in osteoporotic bone defect. *Acta Biomater.* **2024**, *180*, 82–103.

[24] Zou, B. H.; Xiong, Z. S.; He, L. Z.; Chen, T. F. Reversing breast cancer bone metastasis by metal organic framework-capped nanotherapeutics via suppressing osteoclastogenesis. *Biomaterials* **2022**, *285*, 121549.

[25] Zou, B. H.; Xiong, Z. S.; Yu, Y. Z.; Shi, S. J.; Li, X. L.; Chen, T. F. Rapid selenoprotein activation by selenium nanoparticles to suppresses osteoclastogenesis and pathological bone loss. *Adv. Mater.* **2024**, *36*, 2401620.

[26] Yang, M. J.; Tang, Z. Y.; Li, X. Y.; Yu, Y. Z.; He, L. Z.; Chen, T. F. Designing macrophage membrane-engineered ruthenium/selenium nanoparticles to block bone metastasis of breast cancer. *Nano Res.* **2024**, *17*, 7504–7512.

[27] Adadi, P.; Barakova, N. V.; Muravyov, K. Y.; Krivoshapkina, E. F. Designing selenium functional foods and beverages: A review. *Food Res. Int.* **2019**, *120*, 708–725.

[28] Yu, Y. Z.; Xie, B.; Wang, J. L.; Luo, W. Z.; Yang, M. J.; Xiong, Z. S.; Huang, G. N.; Yang, J. W.; Tang, Z. Y.; Qiao, R. et al. Translational selenium nanoparticles promotes clinical non-small-cell lung cancer chemotherapy via activating selenoprotein-driven immune manipulation. *Adv. Mater.* **2025**, *37*, 2415818.

[29] Hou, Y. H.; Wang, W. G.; Bartolo, P. A concise review on the role of selenium for bone cancer applications. *Bone* **2021**, *149*, 115974.

[30] He, L. Z.; Zhang, Z. H.; Tang, Z. Y.; Shen, K.; Sang, C. C.; Zheng, L.; Xiong, Z. S.; Chen, T. F. Industrial-level production of ultrastable selenium nanoparticles using a confined coordination synthetic strategy. *Cell Rep. Phys. Sci.* **2024**, *5*, 102303.

[31] Dai, H. X.; Fan, Q.; Wang, C. Recent applications of immunomodulatory biomaterials for disease immunotherapy. *Exploration* **2022**, *2*, 20210157.

[32] Wang, H.; Wang, B. B.; Jiang, J.; Wu, Y.; Song, A. N.; Wang, X. Y.; Yao, C. L.; Dai, H. X.; Xu, J. L.; Zhang, Y. et al. SnSe nanosheets mimic lactate dehydrogenase to reverse tumor acid microenvironment metabolism for enhancement of tumor therapy. *Molecules* **2022**, *27*, 8552.

[33] Menon, S.; Salhotra, A.; Shailendra, S.; Tevlin, R.; Ransom, R. C.; Januszyk, M.; Chan, C. K. F.; Behr, B.; Wan, D. C.; Longaker, M. T. et al. Skeletal stem and progenitor cells maintain cranial suture patency and prevent craniosynostosis. *Nat. Commun.* **2021**, *12*, 4640.

[34] Lee, S. C.; Lee, N. H.; Patel, K. D.; Jang, T. S.; Knowles, J. C.; Kim, H. W.; Lee, H. H.; Lee, J. H. The effect of selenium nanoparticles on the osteogenic differentiation of MC3T3-E1 cells. *Nanomaterials* **2021**, *11*, 557.

[35] Nakamura, H.; Hoshino, Y.; Okuyama, H.; Matsuo, Y.; Yodoi, J. Thioredoxin 1 delivery as new therapeutics. *Adv. Drug Deliv. Rev.* **2009**, *61*, 303–309.

[36] Chen, Y. F.; Xu, R. H.; Xie, B.; Ma, L.; He, Y. N.; Liu, H. M.; Chen, T. F. Ultrasound-driven selenium nanoparticles realize bone defect repair through activating selenoproteins to regulate PI3K/AKT signaling pathway. *ACS Nano* **2025**, *19*, 18256–18269.

[37] Zhu, W.; Wang, X. R.; Du, S. Q.; Yan, C. Q.; Yang, N. N.; Lin, L. L.; Shi, G. X.; Liu, C. Z. Anti-oxidative and anti-apoptotic effects of acupuncture: Role of thioredoxin-1 in the hippocampus of vascular dementia rats. *Neuroscience* **2018**, *379*, 281–291.

[38] Tanaka, K. I.; Shimoda, M.; Chuang, V. T. G.; Nishida, K.; Kawahara, M.; Ishida, T.; Otagiri, M.; Maruyama, T.; Ishima, Y. Thioredoxin-albumin fusion protein prevents copper enhanced zinc-induced neurotoxicity via its antioxidative activity. *Int. J. Pharm.* **2018**, *535*, 140–147.

[39] Ito, S.; Minamizaki, T.; Kohno, S.; Sotomaru, Y.; Kitaura, Y.; Ohba, S.; Sugiyama, T.; Aubin, J. E.; Tanimoto, K.; Yoshiko, Y. Overexpression of miR-125b in osteoblasts improves age-related changes in bone mass and quality through suppression of osteoclast formation. *Int. J. Mol. Sci.* **2021**, *22*, 6745.

[40] Kim, K. J.; Lee, J.; Wang, W. H.; Lee, Y.; Oh, E.; Park, K. H.; Park, C.; Woo, G. E.; Son, Y. J.; Kang, H. Austalide K from the fungus *Penicillium rudallense* prevents LPS-induced bone loss in mice by inhibiting osteoclast differentiation and promoting osteoblast differentiation. *Int. J. Mol. Sci.* **2021**, *22*, 5493.

[41] Li, X. Q.; Kou, Y. F.; Jia, J.; Liu, M. C.; Gao, R. Z.; Li, Y. H.; Li, G.; Xu, S. G.; Song, W.; Xie, Y. et al. Phenylboronic-tannin nanocolloids that scavenge subchondral reactive oxygen microenvironment and inhibit RANKL induced osteoclastogenesis for osteoarthritis treatment. *Nano Res.* **2024**, *17*, 9898–9907.

[42] Yang, L.; An, X. Y.; Gong, W.; Wu, W. S.; Liu, B.; Shao, X. Y.; Xian, Y. S.; Peng, R.; Guo, B. S.; Jiang, Q. Liposomal α-cyperone targeting bone resorption surfaces suppresses osteoclast differentiation and osteoporosis progression via the PI3K/Akt axis. *Nano Res.* **2024**, *17*, 2949–2959.